The Cryosphere, 18, 3571–3590, 2024 https://doi.org/10.5194/tc-18-3571-2024 © Author(s) 2024. This work is distributed under the Creative Commons Attribution 4.0 License.





Improved records of glacier flow instabilities using customized NASA autoRIFT (CautoRIFT) applied to PlanetScope imagery

Jukes Liu, Madeline Gendreau, Ellyn Mary Enderlin, and Rainey Aberle

Department of Geosciences, Boise State University, Boise, ID, USA

Correspondence: Jukes Liu (jukesliu@boisestate.edu)

Received: 8 February 2024 – Discussion started: 22 February 2024

Revised: 31 May 2024 - Accepted: 21 June 2024 - Published: 15 August 2024

Abstract. En masse application of feature tracking algorithms to satellite image pairs has produced records of glacier surface velocities with global coverage, revolutionizing the understanding of global glacier change. However, glacier velocity records are sometimes incomplete due to gaps in the cloud-free satellite image record (for optical images) and failure of standard feature tracking parameters, e.g., search range, chip size, or estimated displacement, to capture rapid changes in glacier velocity. Here, we present a pipeline for pre-processing commercial high-resolution daily PlanetScope surface reflectance images and for generating georeferenced glacier velocity maps using NASA's autonomous Repeat Image Feature Tracking (autoRIFT) algorithm with customized parameters. We compare our velocity time series to the NASA Inter-Mission Time Series of Land Ice Velocity and Elevation (ITS_LIVE) global glacier velocity dataset, which is produced using autoRIFT, with regional-scale feature tracking parameters. Using five surge-type glaciers as test sites, we demonstrate that the use of customized feature tracking parameters for each glacier improves upon the velocity record provided by ITS_LIVE during periods of rapid glacier acceleration (i.e., changes greater than several meters per day over 2-3 months). We show that ITS_LIVE can fail to capture velocities during glacier surges but that both the use of custom autoRIFT parameters and the inclusion of PlanetScope imagery can capture the progression of orderof-magnitude changes in flow speed with median uncertainties of $< 0.5 \,\mathrm{m}\,\mathrm{d}^{-1}$. Additionally, the PlanetScope image record approximately doubles the amount of optical cloudfree imagery available for each glacier and the number of velocity maps produced outside of the months affected by darkness (i.e., polar night), augmenting the ITS_LIVE record. We demonstrate that these pipelines provide additional insights into speedup behavior for the test glaciers and recommend that they are used for studies that aim to capture glacier velocity change at sub-monthly timescales and with greater spatial detail.

1 Introduction

Feature tracking in optical images is broadly used to measure the displacement of the Earth's surface over time and requires identification of matching visual features between images collected at different times. When applied to repeat-pass satellite images, it can be used for image coregistration (Sommervold et al., 2023) or tracking of ground or ice surface motion (Van Wyk de Vries et al., 2022). We focus on its applications for tracking glacier surface velocities, although the processing method we present may be more broadly applied.

Feature tracking in optical satellite images has been used to measure ice velocity at scales ranging from individual sites to entire regions (Van Wyk de Vries and Wickert, 2021; Howat, 2020; Gardner et al., 2023). The NASA Making Earth System Data Records for Use in Research Environments (MEaSUREs) Inter-Mission Time Series of Land Ice Velocity and Elevation (ITS_LIVE) dataset contains ice velocity time series for the global inventory of glaciers and ice sheets, produced using NASA's autonomous Repeat Image Feature Tracking (autoRIFT) algorithm (Gardner et al., 2018, 2023). autoRIFT is a fast, 2D normalized cross-correlation technique that can be applied to time series of optical images from Sentinel-2 and Landsat as well as synthetic aperture radar (SAR) images from Sentinel-1 (Lei et al., 2021). In each image pair, the second (i.e., later) im-

age is divided into patches called chips, which are matched within a search range to the first/reference image by identifying the peak normalized cross-correlation value (Lei et al., 2021). AutoRIFT iteratively tests larger chip sizes until feature displacements are successfully identified. AutoRIFT applies a normalized displacement coherence filter to identify and remove low-coherence displacement results based on displacement thresholds that are scaled to the local search range (Lei et al., 2021). The additional use of autoRIFT's sister package, Geogrid, geocodes autoRIFT's displacement outputs and allows for the creation of georeferenced velocity maps (Lei et al., 2021).

Successful feature tracking by ITS_LIVE is facilitated by the iterative identification of the ideal chip size as described above, incorporation of all image pairs with acquisition dates ≤ 545 d apart, and the use of regional-scale downstream search ranges identified using reference velocities (Gardner et al., 2023). However, for glaciers with large changes in speed on seasonal to multiyear timescales, the use of static reference velocity maps results in failed feature identification if the actual displacements far exceed the reference velocities, as shown in Liu et al. (2024a) and in the examples we present here. Gaps in glacier velocity records hinder the study of a variety of speedup behaviors that provide insight into internally driven (Liu et al., 2024a; Beaud et al., 2022; Benn et al., 2023; Paul et al., 2022) and externally forced (King et al., 2020) changes in glacier velocity.

One way to increase the amount of velocity data produced through autoRIFT is to customize the search ranges and chip sizes for each glacier, as done in Liu et al. (2024a). Another strategy is to apply autoRIFT to other image products such as the approximately daily high-resolution (< 5 m) optical imagery from the PlanetScope (PS) satellite constellation. Three active PS satellite generations totaling more than 170 satellites collect visible and near-infrared observations at various times throughout the day, enabling daily repeats for \sim 90 % of the Earth's land (PBC, 2022; Roy et al., 2021).

Although the PS images have superior temporal resolution compared to the government-owned images traditionally used for feature tracking (i.e., Landsat and Sentinel-2), use of these images can be challenging. Unlike the standard Landsat and Sentinel-2 products, there are inconsistencies in PS image radiometry (Leach et al., 2019; Frazier and Hemingway, 2021; Latte and Lejeune, 2020; Kington and Collison, 2022) between satellites as well as differences in local overpass times and image spatial resolution (3.0-4.2 m) across generations of satellites (Roy et al., 2021; PBC, 2022). Additionally, the relatively small footprints provided often require mosaicking of multiple images to cover the full study area, which can result in inaccurate displacements across image mosaics due to coregistration errors (Leach et al., 2019; Frazier and Hemingway, 2021; Latte and Lejeune, 2020). Furthermore, the proportion of images with standard quality (i.e., sun altitude $\geq 10^{\circ}$, off-nadir view angle less than 20° , and $\leq 20\%$ saturated pixels) is substantially lower in many glacierized regions because they tend to be located at relatively high latitudes where cloud and snow cover adversely impact geolocation and spectral response accuracies (Roy et al., 2021). Even for the same satellite, there may be substantial variation in the surface reflectance values between images, especially in challenging lighting conditions (i.e., low sun angles, large changes in topographic shading from steep terrain, and saturation over bright features such as snow and glaciers; Kington and Collison, 2022). Here, we present a pre-processing method to address these challenges and standardize the PS imagery for use in optical feature tracking with autoRIFT using customized parameters, which we refer to as "CautoRIFT", for custom autoRIFT.

We apply the CautoRIFT pipeline to Sentinel-2, Landsat 8 and 9, and the pre-processed PS images for five glaciers in a wide range of geographic and climate settings that are known to have periodic variations in speed of 1 order of magnitude or greater (i.e., surges) in order to assess the performance of the modified velocity-mapping pipeline. We demonstrate that the use of PS imagery, processed with customized autoRIFT parameters, may be harnessed to increase the temporal coverage of glacier velocity data during periods of rapid flow speed variability.

2 Methods

Here, we describe the required inputs and steps of the PS CautoRIFT pipeline for mapping glacier velocities. We apply the pipeline to five surge-type glaciers from a range of geographic and climatic settings: Aavatsmarkbreen in Svalbard, Sít' Kusá (Turner Glacier) in Alaska, Nàłùdäy (Lowell Glacier) in Yukon, Medvezhiy Glacier in the Pamir Mountains, and South Rimo Glacier in the Karakoram. For each glacier, we map surface velocities over a \sim 2-year period and compare the results to CautoRIFT velocities produced from Sentinel-2 and Landsat image pairs over the same time period, as well as to the ITS_LIVE velocity record.

2.1 Inputs

The inputs for the PS CautoRIFT pipeline include the preprocessed PS images, several geospatial files specific to the study site, and parameters for the CautoRIFT algorithm as described below.

The PS image record has daily resolution starting in 2014 with the launch of the PS2 instruments, increasing in temporal resolution over time. Following the launches of PS2.SD in 2019 and PSB.SD in 2020, the image record achieves subdaily resolution (PBC, 2022). The constellation's spatial coverage ranges from $\pm 81.5^{\circ}$ depending on the season, with more overlap in the high latitudes due to the satellites' sunsynchronous orbits (PBC, 2022; Roy et al., 2021). PS images acquired in darkness are not processed and are excluded from the databases because they cannot be geolocated, resulting in

seasonal temporal gaps at high latitudes (Roy et al., 2021). For a midlatitude study site of 20 km × 30 km in size, for example, 200–800 GB of downloadable imagery may be available for a 2-year period. For a site with consistent near-daily coverage and an average of eight tiles per day (see Fig. 2), there can be > 5000 image tiles. We use the Sentinel-2 (S2) harmonized and normalized data, which are generated by fitting a non-linear model that transforms the input PS scene's reflectance coefficients to match the S2 spectral response from an S2-based seasonal reference dataset, minimizing large deviations between scenes from differences in daylight and ambient conditions (Kington and Collison, 2022). Harmonization and normalization reduces the differences in surface reflectance between scenes due to variation in lighting conditions, especially due to low sun angles, large changes in topographic shading from steep terrain, and saturation over bright features such as snow and glaciers (Kington and Collison, 2022). Normalization of PS images by Planet Labs may deteriorate the absolute radiometric accuracy but provides increased consistency when comparing different images (Kington and Collison, 2022).

The auxiliary geospatial file inputs for each glacier site include (1) a glacier outline shapefile, (2) an area of interest (AOI) shapefile, (3) a digital elevation model (DEM) covering the AOI, and (4) a 5 m resolution GeoTIFF file covering the AOI to standardize the spatial resolution of all images (Fig. 1). The glacier outline can be downloaded from the Global Land Ice Measurements from Space database with the Randolph Glacier Inventory (RGI; Working Group on the Randolph Glacier Inventory and Infrastructure for Glacier Monitoring, 2017) or manually delineated. The glacier outline may need to be modified to be a 2D single-layer shapefile with the projection that matches the imagery. The AOI shapefile should be a rectangular polygon that covers the glacier and surrounding land. All downloaded images will be cropped to this AOI. The glacier outline and AOI can be cropped to cover only the portion of the glacier that is of interest to reduce computation time for larger glaciers. The DEM is used to guide the down-slope search in the autoRIFT algorithm and for georeferencing the output velocity map (Gardner et al., 2023). The DEMs used in this study are listed in Table 1. The 5 m resolution GeoTIFF is solely used to standardize the spatial resolution and grid of all downloaded PS images. Here we use 30 m resolution Landsat surface reflectance images resampled to 5 m using the GRASS v7.8.6 r.resamp.rst function in QGIS (Landa et al., 2021), which re-interpolates the image using a regularized spline with tension and smoothing. One could instead re-use the DEM resampled to 5 m resolution or any other gridded GeoTIFF.

Optional inputs for the CautoRIFT pipeline include a reference velocity map and a stable surface mask. Search ranges can be adjusted manually using a scaling factor or automatically using the reference velocity map, which must be input as separate *x* direction and *y* direction velocity files. A

stable surface mask can be generated automatically through the pipeline using the glacier outline and AOI polygon but may require manual editing to exclude any other bodies of ice within the AOI and outside of the glacier outline. The mask is a binary raster, where 1 values represent stable surfaces, and 0 values represent all other pixels within the AOI. The script generate_stable_surface_mask will automatically generate the mask as the inverse of the glacier outline provided as input with the same extent as the AOI. Other glaciers and/or ice mélange present in the AOI outside of the glacier outline must be manually removed from the stable surface mask. We manually edited our stable surface masks to remove other glacier ice within the AOIs using QGIS. The stable surface mask will mask out any velocities over static surfaces surrounding the glacier if included as an input to autoRIFT. However, we used the masks in post-processing to calculate the stable surface error (SSE) associated with each velocity map, using calculate_vmap_SSE, as was done in Nolan et al. (2021) and Liu et al. (2024a). The SSE is equal to the root mean squared error (RMSE) in speed from all stable surface pixels according to the stable surface mask.

2.2 Pipeline

The PS pre-processing and CautoRIFT pipeline is summarized in Fig. 1. The PS image pre-processing steps are contained in a GitHub repository named planet_tile2img (Liu et al., 2024b), while the CautoRIFT steps are contained in a GitHub repository named CautoRIFT (Liu, 2024). Landsat (LS) and Sentinel-2 (S2) images cropped to the AOI can be directly input to the CautoRIFT steps. Scripts to download and crop these other satellite images are also provided in the CautoRIFT repository.

The PS images must first be downloaded through either the Planet Explorer or a Planet API. Image download requires a Planet Labs account and its associated API key. Free access to a Planet Labs account is provided through the NASA Commercial SmallSat Data Acquisition Program. Here, we download S2-harmonized images (see Sect. 2.1) through the Planet API. Cloudy images can be filtered before downloading using a cloud cover threshold, calculated with the provided cloud masks. We used the near infrared (NIR) images because the band range and width are the most consistent across the three PS satellite generations and correspond most closely to the S2 band range and width (PBC, 2022). The NIR images are downloaded as individual "tiles", which must be stitched along-track for each satellite overpass. The downloads and subsequent pre-processing steps are applied to monthly batches of images, which are split into directories named by their date, in YYYY-MM format. The download step may fail due to the API connection timeout if a large number of tiles are available for the month. We provide an optional half-month alternative for the download script, but users must manually consolidate the directories for each

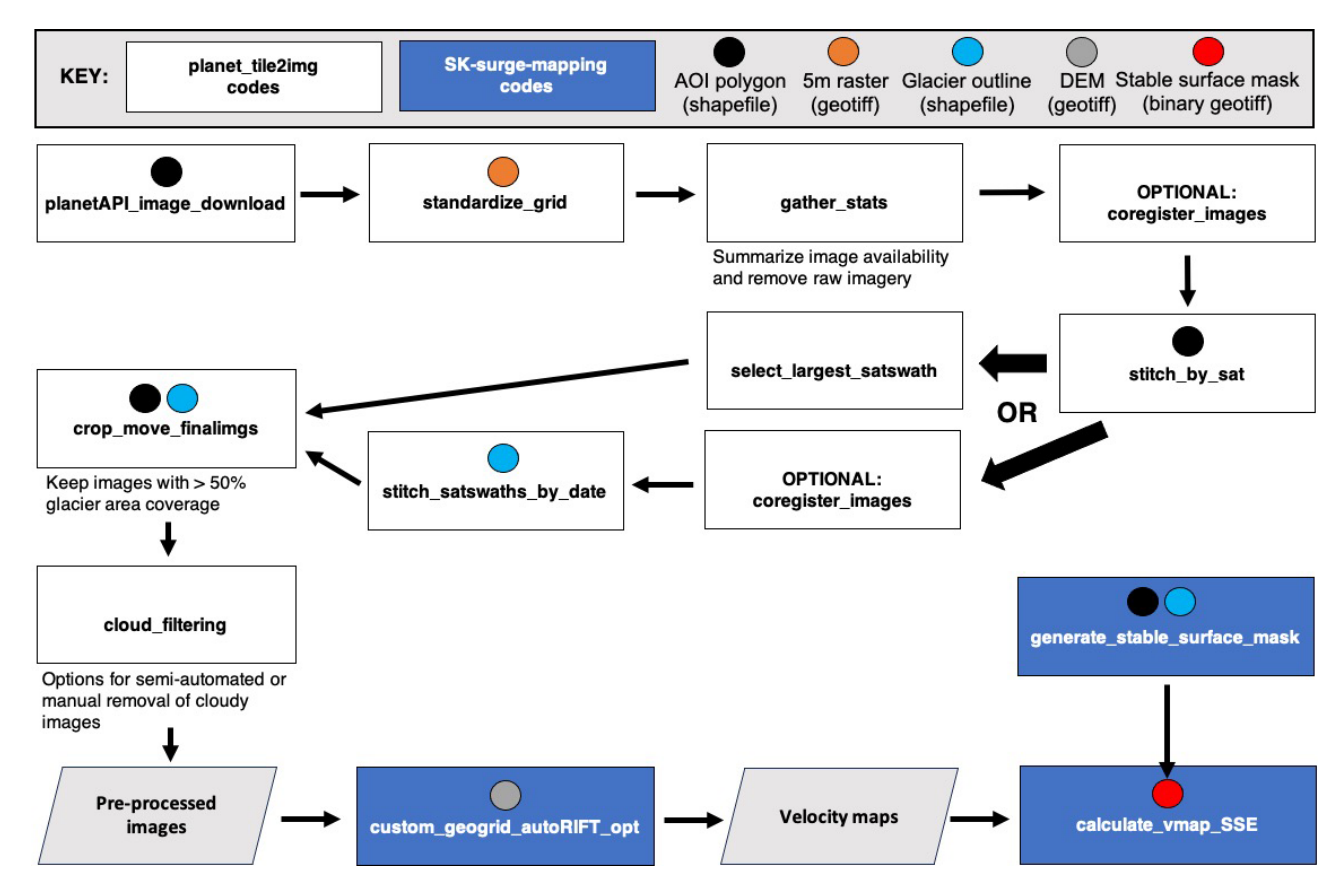


Figure 1. Flowchart of the pipeline for processing PlanetScope imagery for input to CautoRIFT. Each of the rectangles corresponds to a Python script in either the planet_tile2img or CautoRIFT code repository, distinguished by rectangle color. The circles within the rectangles correspond to an input for that script.

month to proceed with the following steps using the existing code.

Following bulk image download, all the image tiles are resampled to the 5 m grid of the input GeoTIFF using a linear spline interpolation in order to standardize the spatial grid (standardize_grid). Then, we record the number of tiles available and satellite overpasses (i.e., swaths) each day of the month to characterize image availability for the month (gather_stats). Since only the resampled files are used in subsequent steps, we remove the raw files to reduce storage needs.

The resampled image tiles are stitched along-track for each satellite, producing a "satellite swath" associated with the acquisition date and PS satellite ID. The PS images are coregistered with the accuracy of 10 m RMSE at the 90th percentile (PBC, 2022), and some of the image tiles may not stitch together smoothly due to errors in image georeferencing. Thus, there is an optional coregistration step (coregister_images), which performs a 2D cross-correlation of the images and finds the x and y offset that correspond to the maximum normalized correlation value. For each pair of overlapping image tiles, if the correlation value is above the correlation threshold (default 0.8) and the x and

y offset are less than the offset threshold (default 2 pixels, or 10 m), then the second image will be shifted accordingly (Fig. 2). All coregistration thresholds can be adjusted manually within the pipeline.

In the case where multiple satellite swaths overlap on a single day, either one swath can be selected or the overlapping swaths can be mosaicked to increase spatial coverage. Here we mosaicked all satellite swaths for each day in order to maximize the spatial coverage of the imagery using stitch_satswaths_by_date. The acquisition time for overlapping swaths can differ by seconds to hours (Roy et al., 2021), which can impact the consistency in brightness between the images, even after pre-processing. Within the region of swath overlap, the mean brightness difference is used to uniformly adjust the brightness values in the smaller swath in order to minimize brightness bias between swaths. Another option available through the pipeline is to select one swath per day using select_largest_satswath. By default, the swath with the greatest spatial coverage within the AOI is selected if only using a single swath for a date. Alternatively, the user can manually select the best swath by copying its file into the directory containing the final images for each date. Figure 2 demonstrates the process for both sce-

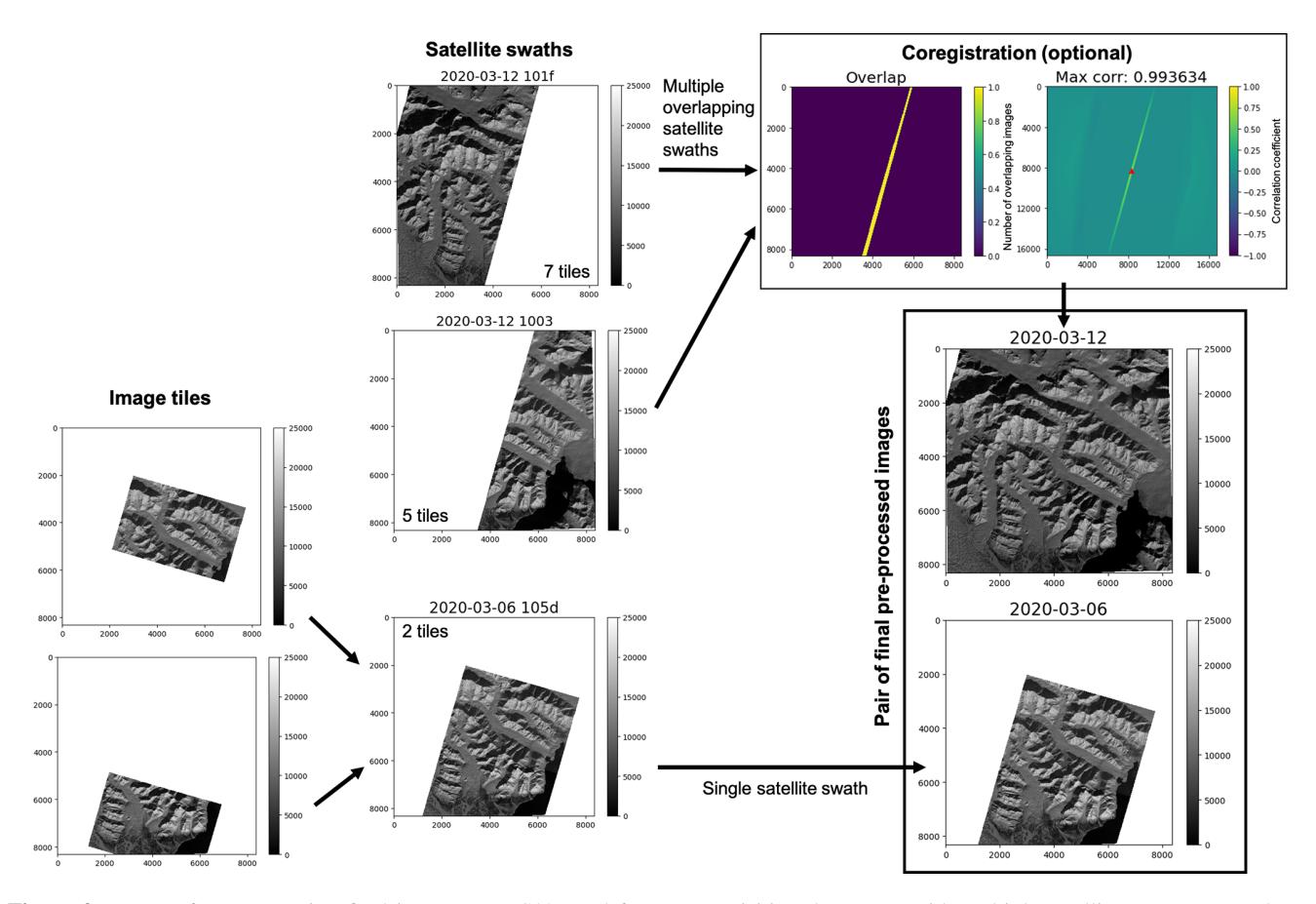


Figure 2. Process for constructing final images over Sít' Kusá for two acquisition dates, one with multiple satellite overpasses and one with a single overpass. The color map for all grayscale plots corresponds to the image pixel intensity. The satellite swaths are labeled by acquisition date and four-digit satellite ID. The number of tiles corresponding to each swath are listed in the corner of each swath image. The tiles for the 12 March 2020 swaths are not shown due to space limitations. The red triangle in the 2D cross correlogram associated with the optional coregistration step indicates the offset corresponding to the maximum normalized correlation, 1 and 2 pixels of offset for x and y, respectively, in the example shown here.

narios: selecting a single satellite swath versus stitching together multiple satellite swaths.

Once the single satellite swath or mosaicked swaths for each date are selected, the final images are cropped to the AOI, and the images with greater than 50 % data coverage over the glacier area are automatically moved into a separate directory using the <code>crop_move_finalimgs</code> script. To optimize computation and analysis time, images with clouds covering part or all of the glacier may then be removed. Clouds can be filtered manually or automatically using the script provided (cloud filtering), which automatically plots the images in series to aid in manual filtering but also includes optional steps to test automated filtering methods that rely on gradients in pixel brightness. For the example applications presented herein, we manually filtered cloudy images because the cloud brightness varies widely between sites. Even for images captured at the same site, cloud brightness thresholds need to be calibrated carefully. Based on the test applications presented below, visually checking

and deleting the cloudy images for a 2-year analysis period (up to 550 images for the test sites) required less than 30 min of user effort.

In addition to the final non-cloudy images, the required inputs to CautoRIFT include a DEM over the AOI. The DEM is used to calculate glacier surface slopes to guide the autoRIFT feature tracking search directions. The DEM used for each test site is listed in Table 1. The original resolution and quality of the DEM must capture the relative shape of the glacier surface, but the DEM does not need to be high resolution because it is resampled to the user-specified feature tracking chip sizes in order to be compatible with the autoRIFT workflow. Within the CautoRIFT script, the user must input the chip sizes, which control the spatial resolution of the resulting velocity maps, and minimum and maximum date separations. The input of a reference velocity map automatically sets search ranges based on expected displacements, which is particularly helpful during speedups and for glaciers where there are large spatial variations in speed. In the absence of a reference velocity map, one may manually test different search ranges within the script. The modification of the search range within the script imposes a static search range value to the entire AOI. In this study, a reference velocity map during a glacier surge was only available for Sít' Kusá. We used the velocity map from the 2006 surge from Nolan et al. (2021) as the input. For the other sites, we applied large search ranges of 16 times the input chip size.

2.3 Other velocity data

Sentinel-2 and Landsat 8 and 9 images may also be downloaded and input to the CautoRIFT pipeline. The CautoRIFT repository provides scripts to automatically download Sentinel-2 cloud optimized Geo-TIFF (COG) images and Landsat 8 and 9 Collection 2 Level 1 images through Amazon Web Services (AWS), through Planet Explorer or by adjusting the planetAPI image download script. We downloaded the 10 m resolution NIR band from Sentinel-2 images to match the resolution of the PS imagery. For Landsat 8 and 9, the 15 m resolution panchromatic band was used because it has the highest spatial resolution of all Landsat bands. All images were cropped to the AOI and then filtered for cloud coverage using the same cloud_filtering step as the PS images. These cropped images can be directly input to CautoRIFT.

The ITS_LIVE velocity time series can be extracted for specific point locations using the ITS_LIVE widget (Gardner et al., 2023). The time series include velocities from standard autoRIFT parameters (chip sizes and search ranges determined for an entire region) applied to Sentinel-1, Sentinel-2, and Landsat imagery. The error associated with each ITS_LIVE velocity measurement is calculated from the standard deviation of velocities measured over a stable surface after applying a geolocation offset (Gardner et al., 2023). If the velocity field does not intersect a stable surface, the error is assigned as the residual sum of squares of the satellite pointing uncertainty (i.e., positioning and orientation accuracy) for both images (Gardner et al., 2023).

2.4 Test applications

We chose five glaciers to assess the performance of the CautoRIFT pipeline relative to the ITS_LIVE dataset (Fig. 3). We focused specifically on surge-type glaciers because they represent particularly challenging conditions for feature tracking given their velocity variations of 1 or more orders of magnitude. We included five surge-type glaciers from varying climate regimes and spanning a wide range of latitudes (35–79° N) to account for differences in image quality and quantity in pipeline performance. Three of the study glaciers have surged since 2019: Sít' Kusá (Turner Glacier), Nàłùdäy (Lowell Glacier), and South Rimo Glacier. Sít' Kusá was confirmed to have surged from 2020 to 2021 using in situ

and remotely sensed velocities (Liu et al., 2024a). South Rimo Glacier surged in 2019 (Jiang et al., 2021) and Nàłùdäy surged in the winter of 2023 (Van Wychen et al., 2023) based on inspection of remotely sensed velocities. Table 1 summarizes the previously measured quiescent and surge flow speeds that are used to guide the selection of minimum and maximum date separations used for velocity map processing. The glaciers with continental climates include Nàłùdäy/Lowell Glacier (LO) on the Canadian side of the St. Elias mountain range, Medvezhiy Glacier (MZ) in the Pamir mountains, and South Rimo Glacier (SR) in the Karakoram. The glaciers with maritime climates include Sít' Kusá (SK) on the Alaskan side of the St. Elias mountain range and Aavatsmarkbreen (AV) on Spitsbergen, Svalbard.

We mapped velocities for each test glacier over a 2-year period in order to capture seasonal velocity changes for at least one full season and to capture the full surge for each of the glaciers with confirmed surges. The temporal resolution of the velocity estimates varied between glaciers based on their flow speeds and image availability. Velocities for glaciers with fast flow $(\ge 5 \,\mathrm{m}\,\mathrm{d}^{-1}) - \mathrm{SK}$, LO, and SR – were mapped using image pairs with date separations of 5 to 60 d, as done successfully for SK's surge in Liu et al. (2024a). Velocities for glaciers with slow flow speeds ($\leq 5 \,\mathrm{m}\,\mathrm{d}^{-1}$) – MZ and AV – were mapped with longer date separations of 14 to 60 d in order to successfully detect displacement across the minimum chip sizes and search ranges for autoRIFT. For the PS images, we automatically mosaicked all the satellite swaths for each day. For the sake of computational efficiency, the optional across-swath coregistration was only applied to Medvezhiy Glacier because its small size and relatively slow flow speeds make it susceptible to velocity errors from poor geolocation (Table 1). For our maximum offset threshold of 2 pixels (10 m) and a site with a flow speed of $2 \,\mathrm{m}\,\mathrm{d}^{-1}$ with 14-60 d image pair separations, this corresponds to a maximum coregistration offset correction of 8 % to 35 % of the total displacement. We compared the temporal coverage and quality of the PS, Sentinel-2, and Landsat 8 and 9 CautoRIFT velocity maps produced and assessed how they contribute to the velocity record provided through ITS_LIVE.

3 Results

Here, we summarize the usable image coverage, the quality and characteristics of the CautoRIFT velocity maps, and their improvements to the velocity record provided through ITS_LIVE for the test sites over a \sim 2-year period. Since glacier flow can vary considerably over seasonal and shorter time periods, we take into account variations in image coverage across the boreal winter (December, January, and February), spring (March, April, and May), summer (June, July, and August), and fall (September, October, and November) seasons.

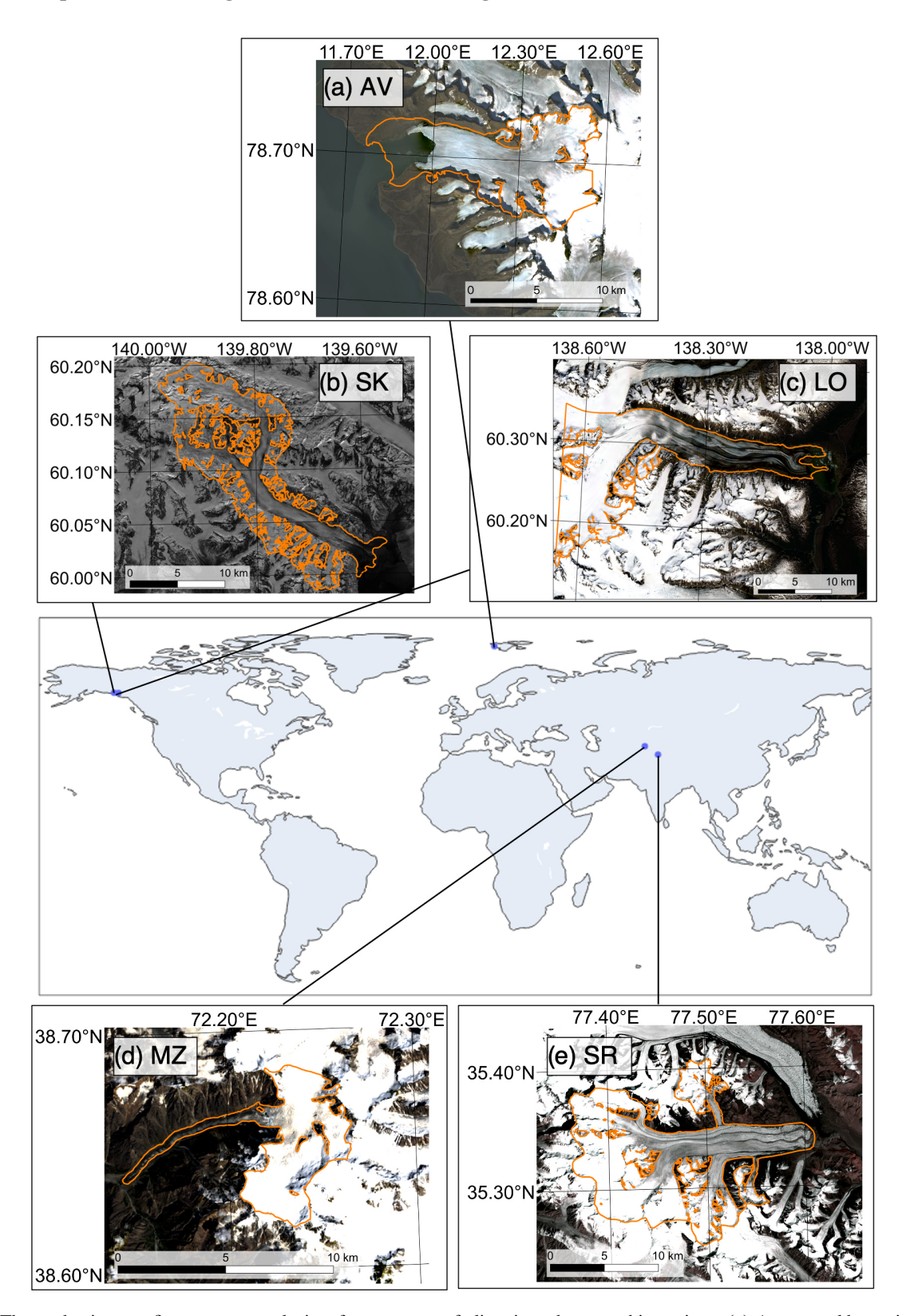


Figure 3. The study sites are five surge-type glaciers from a range of climatic and geographic settings: (a) Aavatsmarkbreen in Svalbard, (b) Sít' Kusá in Alaska, (c) Nàłùdäy in Yukon, (d) Medvezhiy Glacier in the Pamirs, and (e) South Rimo Glacier in the Karakoram. Background images for (a)–(d) are from Landsat 8 and 9. The RGI glacier outlines (orange) may not represent each glacier's current extent.

speeds.						
	Site	Latitude	DEM source	DEM resolution	Oujescent speed	Surge speed

Site	Latitude	DEM source	DEM resolution	Quiescent speed	Surge speed
AV	78.64° N	GMTED2010	52 m	\sim 0.5–0.6 m d $^{-1}$	$4.5\mathrm{m}\mathrm{d}^{-1}$
SK	60.06° N	IfSAR Alaska	5 m	$< 1 - 8 \mathrm{m}\mathrm{d}^{-1}$	$25-30 \mathrm{m}\mathrm{d}^{-1}$
LO	59.97° N	ArcticDEM	10 m	$< 1 \mathrm{m}\mathrm{d}^{-1}$	$30 \mathrm{m}\mathrm{d}^{-1}$
MZ	38.65° N	SRTM	26 m	$\sim 1.5\mathrm{m}\mathrm{d}^{-1}$	$100 \mathrm{m}\mathrm{d}^{-1}$
SR	35.32° N	GTOPO30	27 m	$0.3\mathrm{m}\mathrm{d}^{-1}$	$12{\rm m}{\rm d}^{-1}$

Table 1. Digital elevation models (DEMs) used for study site analysis and other glacier site characteristics, e.g., quiescent and surge flow

In general, higher latitude corresponded to lower image coverage centered around the boreal winter solstice (December 2021 and 2022). Figure 4 shows the availability of noncloudy images for PlanetScope (PS), Sentinel-2 (S2), and Landsat 8 and 9 (LS) for a 2-year period. SR, located in a continental climate and at the lowest latitude of $\sim 35^{\circ}$ N, had the most seasonally consistent record of imagery – at least 18 PS or S2 images for each 3-month season – and the greatest number of winter images: 67 for PS, 41 for S2, and 9 for LS (Fig. 4a). MZ is situated only 3° of latitude higher and had similar image availability to that of SR. MZ had a denser PS and LS image record (247 and 50 images, respectively) overall but slightly fewer winter images (63 PS images; Fig. A1). Due to its similarities to SR, its barcode plot is located in Appendix A. Out of all the sites, velocity maps for the two lowest-latitude sites, MZ and SR, provided the most consistent velocity coverage more than ± 1 month from the winter solstice (Fig. 5). For the sub-Arctic sites, LO and SK, there were fewer images (< 15) each winter because of the longer period of total darkness (i.e., polar night) and/or deep shadows due to low sun angles. Meanwhile, the highest-latitude site, AV, is located in the high Arctic where polar night obscures optical image collection for nearly half the year (from mid-September to March; Fig. 4b). However, during periods of solar illumination (March to mid-September), the increase in satellite track overlap at higher latitudes resulted in a denser record of images available for velocity mapping in comparison to the sub-Arctic sites (Figs. 4, 5a-c).

The sites in maritime climates had lower image coverage due to more frequent cloud cover than continental sites. Although the two sub-Arctic sites, LO and SK, are situated at the same latitude, LO is located in a continental climate zone, whereas SK is located in a maritime climate and has more frequent cloud cover, which reduces the number of usable images by one-third to one-half (Fig. 4). However, the image records for PS and S2 often complemented each other: some S2 images were available in PS image gaps (e.g., spring 2020 and spring 2021) and some PS images were available in S2 image gaps (e.g., fall 2020 and fall 2021; Fig. 4d).

The addition of PS imagery approximately doubled the number of velocity maps produced (Fig. 5) outside of the Arctic, where the S2 and LS coverage was already higher in the summer months unaffected by polar night (Figs. 4b and

5a) due to the increase in orbit overlap at high northern latitudes (Li and Roy, 2017). For the sites other than AV, the temporal resolution provided by the PS imagery was 1.1–3.0 times greater than the coverage provided by S2 imagery, and for SR, MZ, and SK, 1.1–1.8 times greater than the coverage provided by both S2 and LS imagery combined (Figs. 4a, c, d and A1). Notably, the addition of PS imagery increased the number of velocity maps with date separations shorter than 20 d (Fig. 5), which may be advantageous during times of fast flow. For MZ and SR, there were date separations of < 20 d that were only achieved with PS image pairs (Fig. 5d, e). In general, the addition of PS velocity maps produced more uniform monthly velocity coverage, especially in November (Fig. 5b–e).

The CautoRIFT pipeline successfully increased the temporal coverage of velocity observations compared to the ITS_LIVE record and captured higher maximum flow speeds for the four test sites with pronounced seasonal and/or interannual variability. Gaps in the ITS_LIVE record were common during periods of ice acceleration (e.g., Figs. 6b, d, f and 7d), which often occurred when glacier speeds increased above 5 m d⁻¹ (Fig. 6b, d, f). There were gaps during periods of acceleration even when speeds were less than 3 m d⁻¹ (Fig. 7d). Figures 6 and 7 show the ITS_LIVE velocities produced from optical satellite image pairs only, but the equivalent plots that include the Sentinel-1 SAR velocities (shown in Fig. A2) corroborated these observations.

For SK, ITS_LIVE failed to capture velocities from May 2020 through March 2021 (Fig. 6b). In contrast, the CautoRIFT velocities captured the full progression of the 2020-2021 surge for the near-terminus area, tracking the acceleration from $< 1 \,\mathrm{m}\,\mathrm{d}^{-1}$ to $20 + \mathrm{m}\,\mathrm{d}^{-1}$ (Fig. 6b). The additional velocity data revealed the seasonality of velocity change throughout the surge linked to the evolution of glacier hydrology (Liu et al., 2024a). Notably, the inclusion of PS velocity maps captured critical velocity data through October-November 2020 and January-February 2021, filling gaps in the other velocity records during periods of darkness (Fig. 6b). The additional PS velocities confirm that winter velocities remained elevated throughout SK's surge compared to quiescent velocities, as detailed in Liu et al. (2024a). At SR, the ITS_LIVE velocities only captured a peak velocity of $\sim 5 \,\mathrm{m}\,\mathrm{d}^{-1}$ near the glacier terminus (Fig. 6c, d).

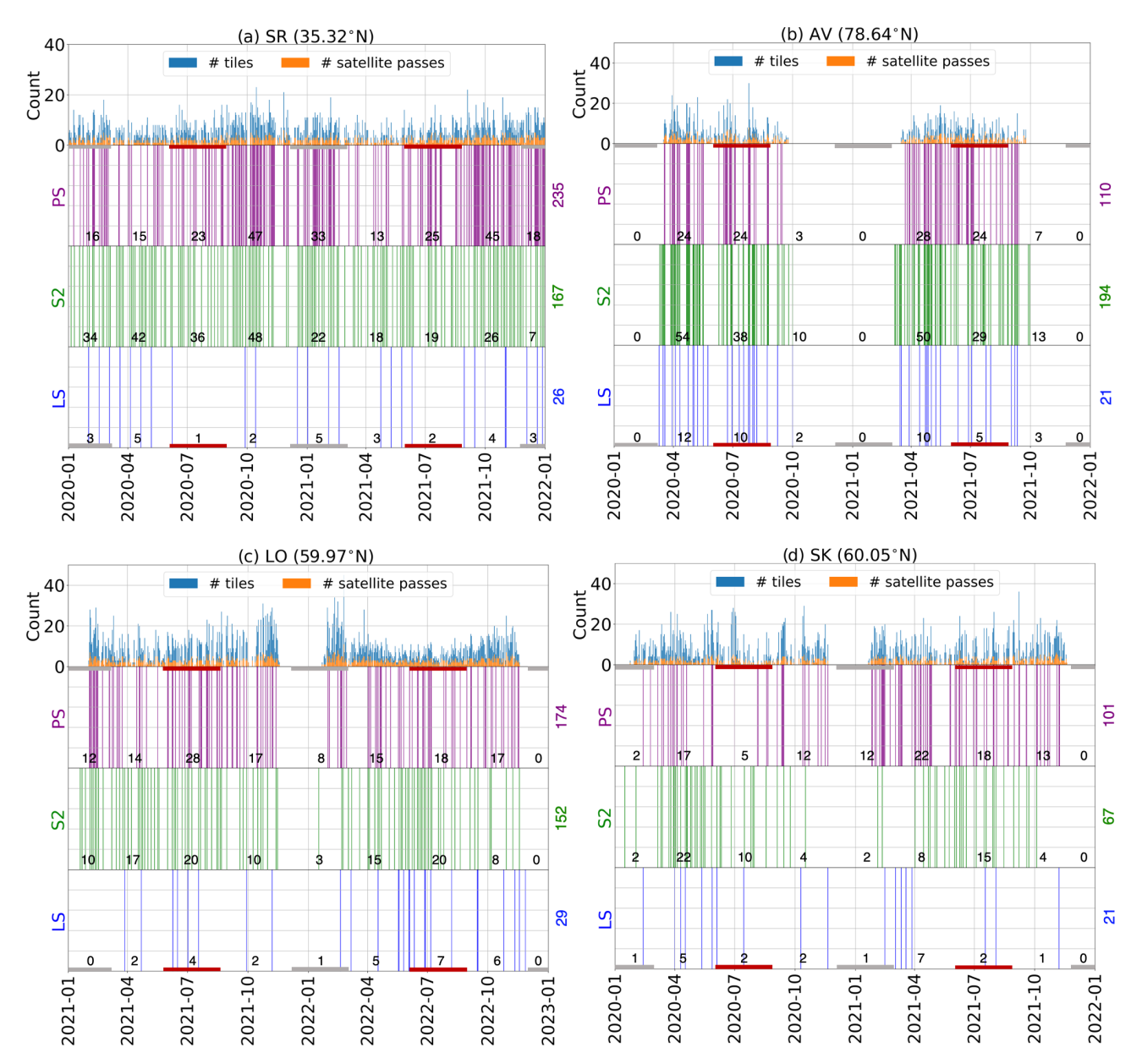


Figure 4. Barcode plots showing cloud-free image availability for the different satellite platforms for four of the study sites over 2 years. See Fig. A1 for the barcode plot for MZ. The left column (**a**, **c**) contains sites in continental climates, while the right column (**b**, **d**) contains sites in maritime climates. The top graph for each site corresponds to the number of tiles and satellite overpasses from the PlanetScope satellites. Red and gray boxes along the bottom and top of the barcodes mark the winter and summer months, respectively. Counts for each season are listed along the barcode, and the total count is shown to the right of the barcode.

LS and PS velocities fill the ITS_LIVE gap from August to October 2019, revealing that velocities reached a peak of nearly 10 m d⁻¹ in August 2019 (Fig. 6d, Table 2), closer to the results derived from SAR feature tracking in Jiang et al. (2021). For LO, ITS_LIVE velocities are sparse from January through August 2022 over the southern branch of the terminus, where the speedup appears to initiate (Fig. 6e, f). The custom S2 and LS velocities capture the rise to the velocity peak and the subsequent decrease, indicating that the

velocities reached between $15\text{--}20\,\text{m}\,\text{d}^{-1}$ (Fig. 6d, Table 2). Similarly at MZ, the CautoRIFT record captures additional portions of the rise and fall from the velocity peak in the main trunk, particularly from April to September 2021 (Fig. 7d, Table 2). At AV, the ITS_LIVE velocity record is quite dense due to the orbit overlap at high latitudes. Because glacier velocities appear to remain steady throughout the study period at $< 1\,\text{m}\,\text{d}^{-1}$ (Fig. 7a, b), the standard autoRIFT parame-

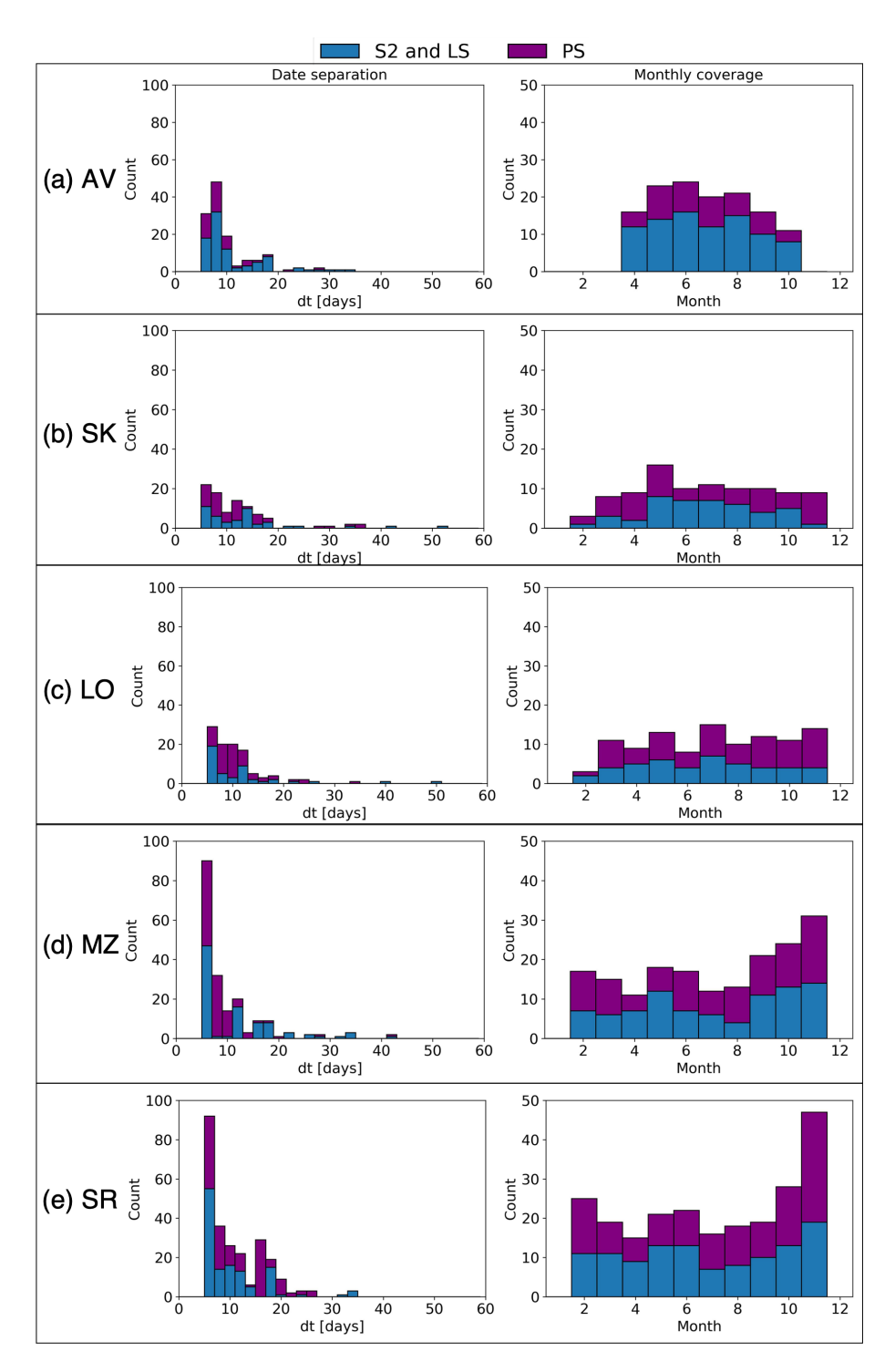


Figure 5. Histograms comparing date separations and monthly coverage for velocity maps from PlanetScope (PS) versus Sentinel-2 (S2) and Landsat (LS) image pairs with date separations between 5 and 60 d for each of the study glaciers. Sites are displayed in order of latitude from north to south.

ters proved successful and the CautoRIFT pipeline does not greatly improve the velocity record for this glacier (Table 2). For all study sites, CautoRIFT achieved median stable surface errors (SSEs) between 0.2 and 0.7 m d⁻¹ for all image

products. The median SSE for the CautoRIFT velocity maps from all the sites was under $0.5 \, \text{m} \, \text{d}^{-1}$, aside from the median LS SSE of $0.7 \, \text{m} \, \text{d}^{-1}$ for AV (Fig. 8). The median SSEs from PS velocity maps ranged from $0.2{-}0.4 \, \text{m} \, \text{d}^{-1}$, which

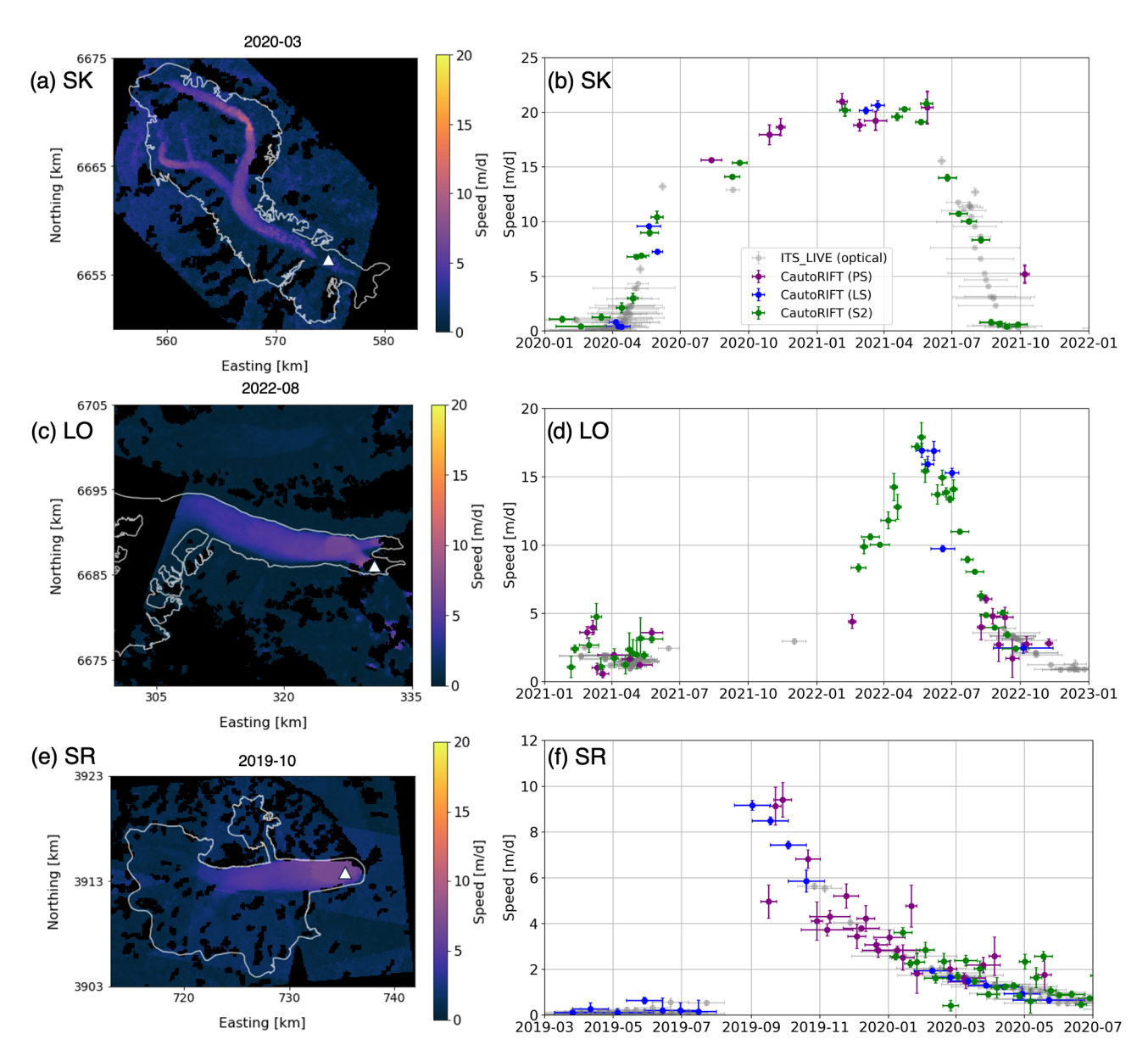


Figure 6. (**a**, **c**, **e**) Example velocity maps produced with the CautoRIFT pipeline applied to PlanetScope (PS), Landsat (LS), and Sentinel-2 (S2) image pairs and (**b**, **d**, **f**) surface speed time series at the point on each glacier marked by the white triangle at SK (**a**, **b**), LO (**c**, **d**), and SR (**e**, **f**). Vertical error bars correspond to the stable surface error for the CautoRIFT data and the provided error values for the ITS_LIVE data, while horizontal error bars mark the date interval for the image pair. Note the different *y*-axis scalings in panels (**b**), (**d**), and (**f**). Date separations of 5 to 60 d were used.

is similar to the median SSEs from S2 $(0.2–0.5\,\mathrm{m\,d^{-1}})$ and lower than the median SSEs from LS for all sites besides SR (Fig. 8). The SSEs from our custom velocity maps were comparable to the SSEs for ITS_LIVE (Fig. 8) despite the use of different stable surface masks between datasets.

4 Discussion

By applying CautoRIFT to the same datasets used to create the ITS_LIVE velocity record (S2 and LS images), our results show that CautoRIFT is needed to capture large variations in glacier velocity. The addition of PS images to CautoRIFT enhances the temporal coverage and resolution of glacier velocity records, yielding accurate velocity maps with high spatial resolution.

For glacier sites that are seasonally velocity-data-limited due to the effects of polar night, the use of PS images can extend the temporal coverage (Fig. 4d) and more than double the number of velocity maps greater than ± 1 month from the winter solstice, especially in the fall months (Fig. 5). The

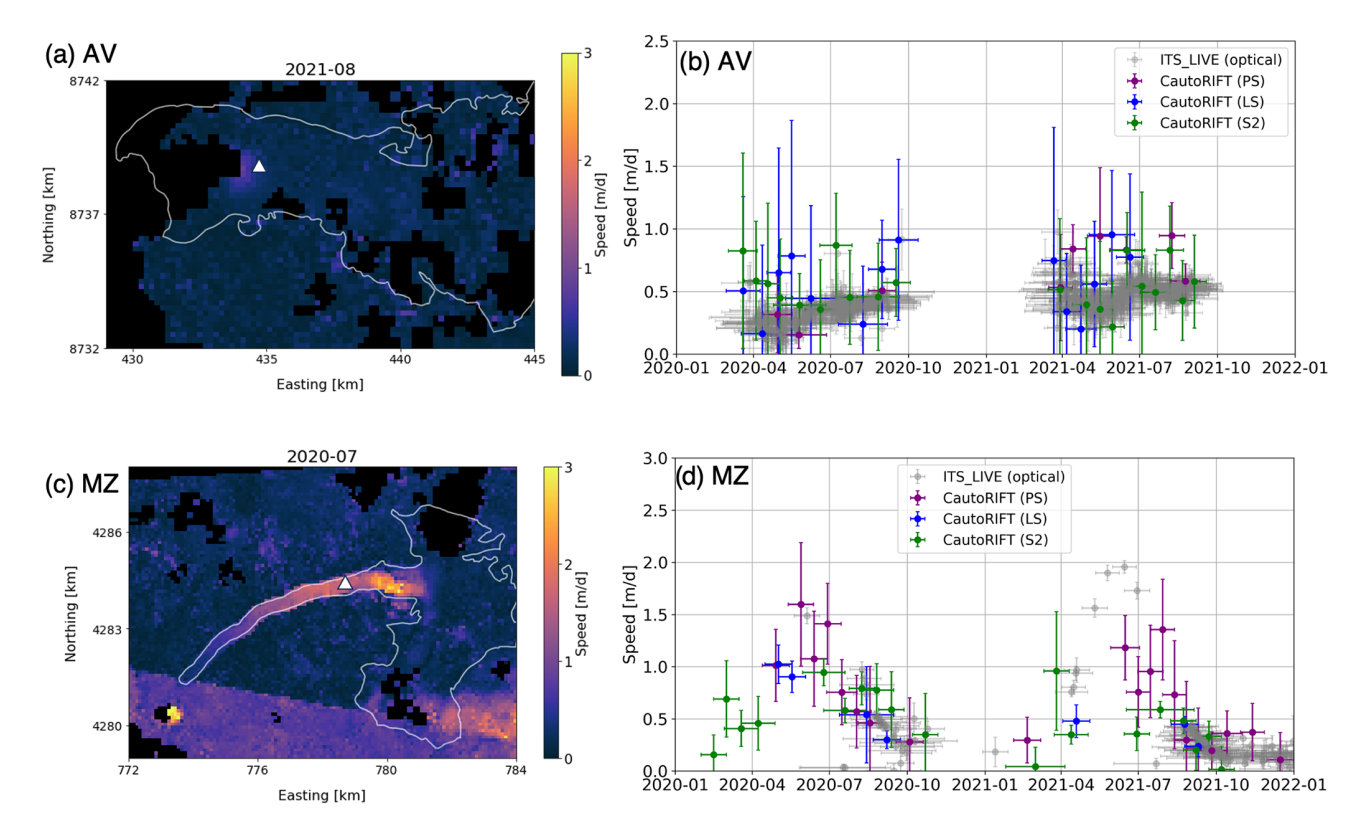


Figure 7. (a, c) Selected velocity maps produced with the CautoRIFT pipeline applied to PlanetScope (PS), Landsat (LS), and Sentinel-2 (S2) image pairs and (**b, d**) surface speed time series at the point on each glacier marked by the white triangle at AV (**a, b**) and MZ (**c, d**). Vertical error bars correspond to the stable surface error for the CautoRIFT data and the provided error values for the ITS_LIVE data, while horizontal error bars mark the date interval for the image pair. Date separations of 14 to 60 d were used.

Table 2. Comparison of ITS_LIVE versus CautoRIFT speedup observations for each glacier site from the velocity time series extracted at the locations shown in Figs. 6 and 7 during the listed speedup time period. Since AV does not experience substantial speedup, the time period chosen corresponds to the period of available optical data for 1 year.

Site	Speedup start	Speedup end	Peak speed		Number of observations	
	[yyyy-mm]	[yyyy-mm]	ITS_LIVE	CautoRIFT	ITS_LIVE	CautoRIFT
AV	2020-04	2020-10	$1 \mathrm{m} \mathrm{d}^{-1}$	$1 \mathrm{m} \mathrm{d}^{-1}$	271	21
SK	2020-05	2021-08	$15 \mathrm{m} \mathrm{d}^{-1}$	$21 \mathrm{m}\mathrm{d}^{-1}$	12	19
LO	2021-10	2022-09	$5 \text{m} \text{d}^{-1}$	$18 \mathrm{m} \mathrm{d}^{-1}$	18	30
MZ	2020-02	2020-09	$2 \text{m} \text{d}^{-1}$	$2 \mathrm{m}\mathrm{d}^{-1}$	15	20
SR	2019-08	2020-04	$6\mathrm{m}\mathrm{d}^{-1}$	$9 \text{m} \text{d}^{-1}$	16	21

inclusion of PS imagery can also increase the velocity map pairings possible at shorter time separations (Fig. 5), which is advantageous for capturing fast glacier flow. Furthermore, CautoRIFT is able to successfully measure velocities during temporal gaps in ITS_LIVE velocities that can occur near the peaks of speedups, typically above speeds of 5 m d⁻¹ (e.g., in Figs. 6 and 7d). Thus, the use of both PS imagery and CautoRIFT can be particularly useful for capturing speedups that initiate in the fall (Abe and Furuya, 2015; Nanni et al., 2023; Liu et al., 2024a), as seen in the SK and SR velocity time series (Fig. 6b, d). While some winter gaps may be

filled with Sentinel-1 SAR imagery, temporal variations in backscatter due to the presence of liquid water prevent its use when and where melt occurs (Marin et al., 2020). Thus, the use of PS images and CautoRIFT may be especially advantageous for glaciers in temperate climate settings where large seasonal velocity fluctuations driven by meltwater input (Burgess et al., 2013; Fountain and Walder, 1998) cause speeds to peak at $> 5 \, \text{m} \, \text{d}^{-1}$ and where liquid water on the surface is more common. Furthermore, for glaciers in maritime climatic settings that are frequently obscured by cloud cover, the use of PS images can improve the temporal cov-

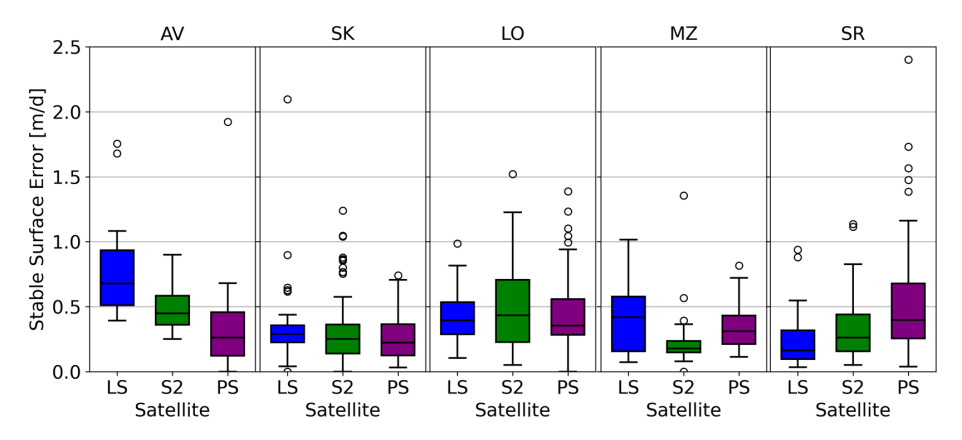


Figure 8. Boxplots showing the calculated stable surface error in velocity maps generated with CautoRIFT using satellite image pairs from different platforms (LS – Landsat, S2 – Sentinel-2, PS – PlanetScope) for each glacier.

erage of velocity records, as demonstrated by the comparison of image availability for LO versus SK (Fig. 4). The inclusion of PS velocity maps can also provide more uniform monthly coverage (Fig. 5b, c). In including PS imagery, however, one must be mindful of some of the artifacts in some of the PS velocity maps due to errors in coregistration and surface reflectance normalization that remain after pre-processing, which show up as seam lines in the velocity maps (e.g., Figs. 6c and 7c). If these boundaries overlap the glacier area, the ice velocities in the overlapping area could be bias corrected by subtracting the velocity offset in the surrounding stable surfaces. Stitching together multiple swaths can increase spatial coverage of the velocity map, but a single satellite swath over the glacier could also be used to reduce errors associated with these boundaries. Both options can be tested within the pipeline to determine which method best balances velocity accuracy and spatial coverage. The coregistration of the PS images could potentially be improved further using a reference S2 image, although this has not been implemented in the published code.

In addition to filling temporal gaps, the use of highresolution PS images to generate glacier velocity maps potentially resolves greater detail in velocity structure relative to S2 and LS velocity maps. Figure 9 illustrates differences in PS and S2 velocity maps from approximately the same time periods. In the case of SK, the PS velocity map showed faster velocities in the upper main trunk and tributaries of the glacier compared to the S2 velocity map, both from late July 2021 (Fig. 9e). The S2 map showed flow speeds near $0 \,\mathrm{m}\,\mathrm{d}^{-1}$ in the northern arm of the glacier, whereas the PS map showed flow speeds of $\sim 5\,\mathrm{m\,d^{-1}}$ in the same area (Fig. 9a, c). GPS data collected throughout field campaigns on SK during its 2020–2021 surge (Liu et al., 2024a; Terleth et al., 2024) confirm that surface speeds in the main trunk were $\sim 6 \,\mathrm{m}\,\mathrm{d}^{-1}$ during July 2021 (Fig. A3). Comparison of the GPS-derived and feature tracking velocities indicate that the PS map matches the GPS velocities more closely than the S2 map (Fig. A3). Thus, the PS velocity map captures a more accurate representation of the velocity of structure of SK. The SSE was also higher for the S2 velocity map $(0.3 \,\mathrm{m}\,\mathrm{d}^{-1})$ compared to the PS SSE of $< 0.1 \,\mathrm{m}\,\mathrm{d}^{-1}$), supporting our interpretation that the PS velocity map provides more accurate glacier velocities in this case. In the case of LO, the speed differences between S2 and PS were $< 0.5 \,\mathrm{m}\,\mathrm{d}^{-1}$ throughout the glacier (Fig. 9f). The greatest velocity deviations occurred where the glacier splits into a northern and southern portion of its terminus as it flows around a bedrock feature (Fig. 9f). There, the PS velocity map provided more continuous spatial coverage of velocities through the two split portions, likely due to the improvements in tracking smaller features provided by the finer spatial resolution in PS images. The large amount of shear strain in this region ($\sim 3 \text{ yr}^{-1}$) may rapidly deform surface crevasses and produce new fractures, as seen in the satellite images, which could hinder accurate feature tracking in that area (Fig. A4). In both the SK and LO examples, S2 minus PS differences were largest along the glacier margins (Fig. 9e, f) since feature tracking with the higher-resolution PS imagery resolves flow closer to the glacier-land (i.e., shear) margin. Since lateral friction is the primary source of flow resistance on fast-flowing outlet glaciers and ice streams (Summers et al., 2023), more accurate characterization of ice flow speed along shear margins can improve estimates of ice discharge. Accurate mapping of ice flow along shear margins may also improve estimates of shear strain heating and thus meltwater production along the margins (Meyer and Minchew, 2018), which is an important meltwater input to the glacier hydrological system that can equal the meltwater flux from frictional heating at the bed (Ranganathan et al., 2023). The improved resolution of velocities along shear margins could also be used to track shear margin migration (Summers et al., 2023).

The improvements to velocity records provided by the inclusion of PS imagery and the CautoRIFT pipeline may yield further insight into rapid changes in glacier dynamics, e.g., to the mechanisms that drive glacier speedup, as in Liu et al. (2024a). Additionally, feature tracking with the high-

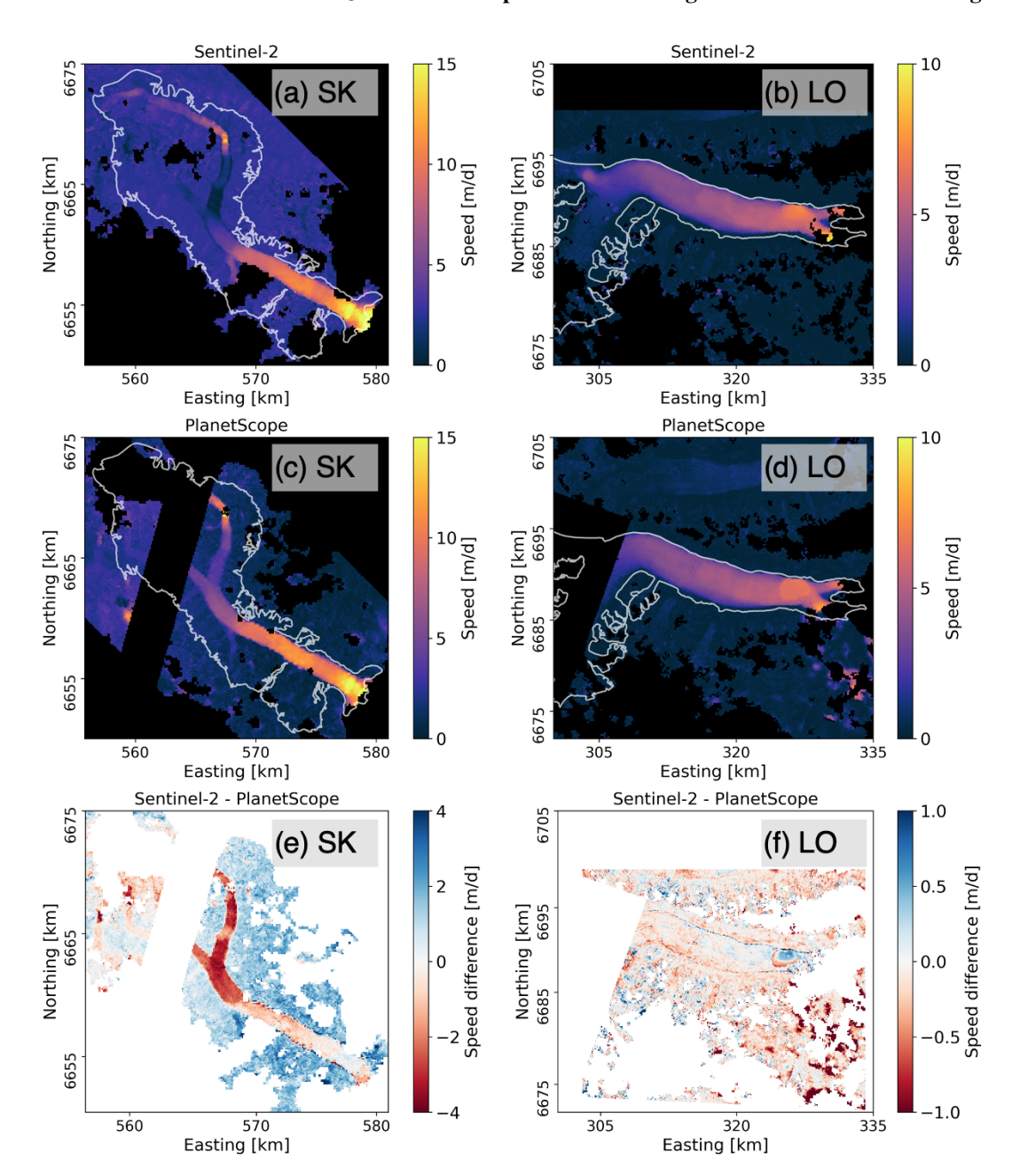


Figure 9. Comparison of detail in velocity maps over SK (**a**, **c**) and LO (**b**, **d**) produced from Sentinel-2 (**a**, **b**) and PlanetScope (**b**, **d**) image pairs. Image pairs have approximately the same dates for each comparison (**a**) 29 July 2021 and 3 August 2021 versus (**b**) 30 July 2021 and 4 August 2021; (**c**) 26 July 2022 and 7 August 2022 versus (**d**) 26 July 2022 and 7 August 2022. PlanetScope speeds are subtracted by Sentinel-2 speeds to calculate speed differences.

resolution PS images may provide more accurate and continuous estimates of velocity structure across the glacier surface. The use of custom parameters in autoRIFT increases the number of velocity maps successfully produced from different sources of optical satellite imagery. These pipelines may be particularly useful for capturing events where dynamic change occurs on monthly or shorter timescales and/or fine spatial scales, such as the kinematic response to drainage of a supraglacial lake or terminus retreat. Finally, improvements

to the ability to successfully map spatial and temporal variations in velocity associated with surges, including surges of narrow tributary glaciers, will yield insight into the heterogeneity of surge behavior (Bhambri et al., 2022) and thus the spectrum of flow instabilities (Herreid and Truffer, 2016).

5 Conclusion

We present a pipeline to pre-process daily high-resolution PlanetScope surface reflectance images and to incorporate the images into the customized autoRIFT feature tracking algorithm for mapping glacier velocities. The pre-processing pipeline performs additional image normalization and coregistration to allow for more seamless mosaicking of image tiles and satellite swaths. The PlanetScope images, along with optical satellite images from Landsat and Sentinel-2, may be used as inputs to the CautoRIFT pipeline with adjustable search parameters and date separations. Using five surge-type glaciers as test sites, we demonstrate that the velocity maps produced with CautoRIFT parameters, along with the inclusion of PlanetScope imagery, can be used to fill gaps in the ITS_LIVE velocity record, which are common when flow speeds rapidly change. The inclusion of PlanetScope imagery approximately doubles the number of velocity maps and is particularly useful for filling gaps in the velocity record for glaciers that are frequently cloud covered. The velocity maps produced with PlanetScope image pairs have stable surface errors that are less than $0.5 \,\mathrm{m}\,\mathrm{d}^{-1}$, which are smaller than the stable surface errors from the Landsat and Sentinel-2 CautoRIFT velocity maps and comparable to the reported ITS_LIVE errors. Furthermore, PlanetScope velocity maps are capable of resolving more continuous velocity structure and with greater spatial detail, including large lateral variations in velocity near the glacier-land margins. The customization of autoRIFT parameters and inclusion of PlanetScope imagery can improve the velocity data coverage from the ITS_LIVE record, especially for glaciers with pronounced seasonal and/or interannual variations in velocity. Both the CautoRIFT pipeline and PlanetScope image preprocessing pipeline produce glacier velocity data that are useful for capturing dynamic change on shorter timescales and over smaller spatial scales. We provide these pipelines as public GitHub repositories for open use and adaptation.

Appendix A: Supplementary material

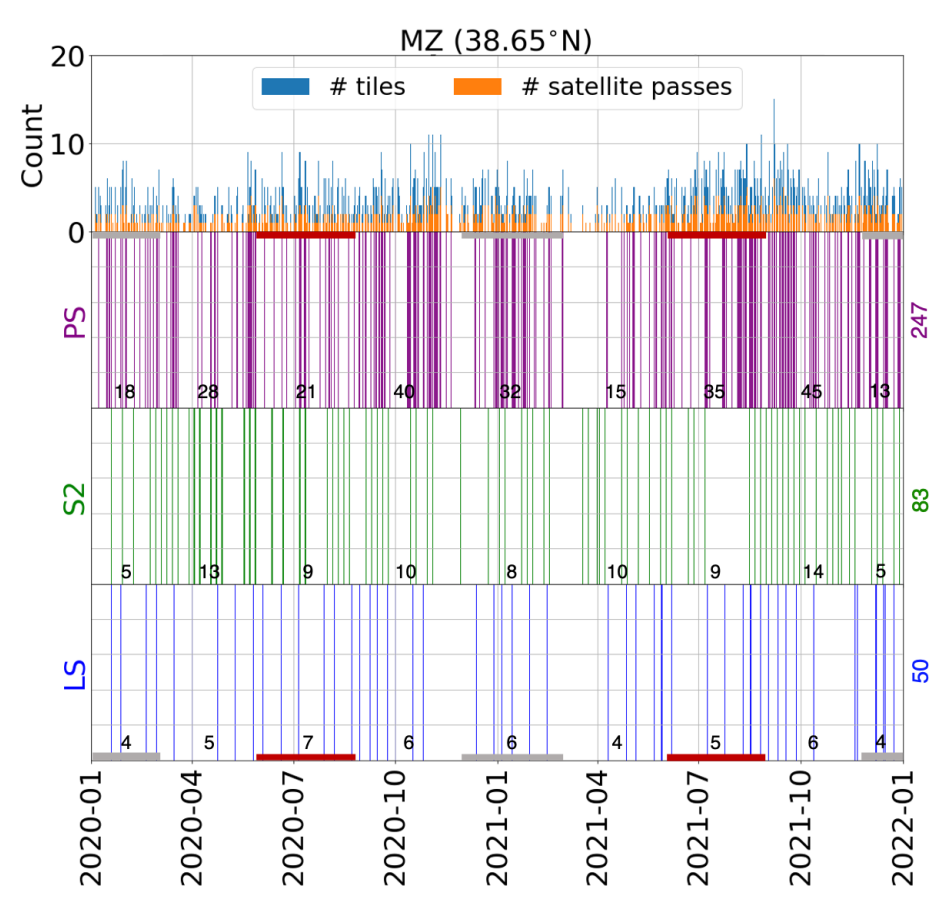


Figure A1. Barcode plot showing cloud-free image availability over Medvezhiy Glacier (MZ) for the three satellite platforms: PlanetScope (PS), Sentinel-2 (S2), and Landsat (LS). Red and gray boxes along the bottom and top of the barcodes mark the winter and summer months, respectively. Counts for each season are listed along the barcode, and the total count for the 2-year period is shown to the right of the barcode.

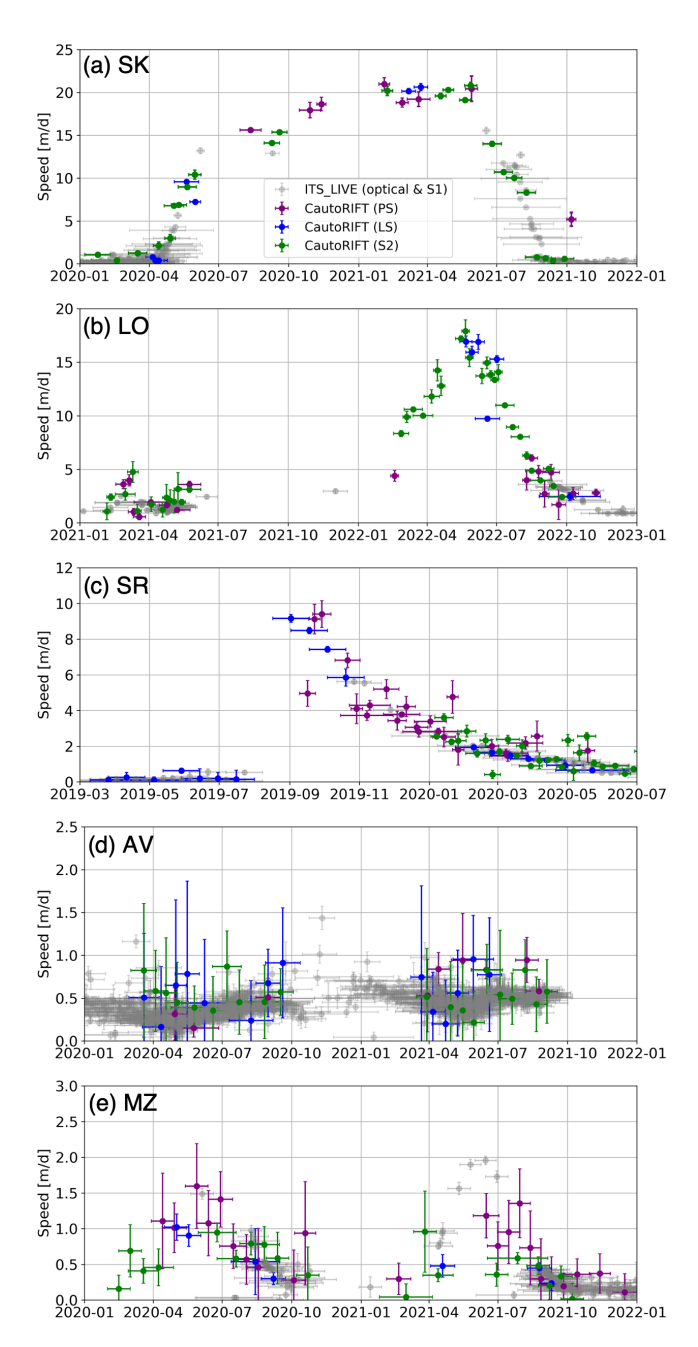


Figure A2. Surface speed time series including Sentinel-1 ITS_LIVE data at the points on each test glacier shown in Figs. 6 and 7. (a) SK, (b) LO, (c) SR, (d) AV, and (e) MZ.

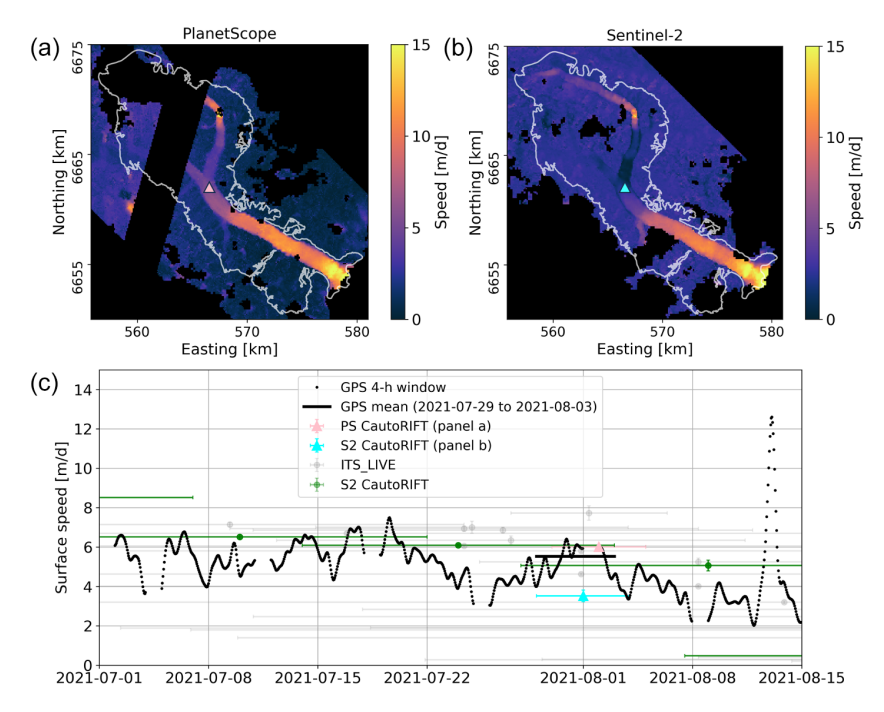


Figure A3. (c) Surface speeds calculated using Precise Point Positioning processing of positions from a Trimble NetR9 GPS with a 4h averaging window at site G15_2106 on Sít' Kusá compared to the velocity map surface speeds at the location of G15_2106 marked by the triangles in panels (a) and (b). The vertical error bars correspond to the SSE for each velocity map, while the horizontal error bars correspond to the date interval for the image pair.

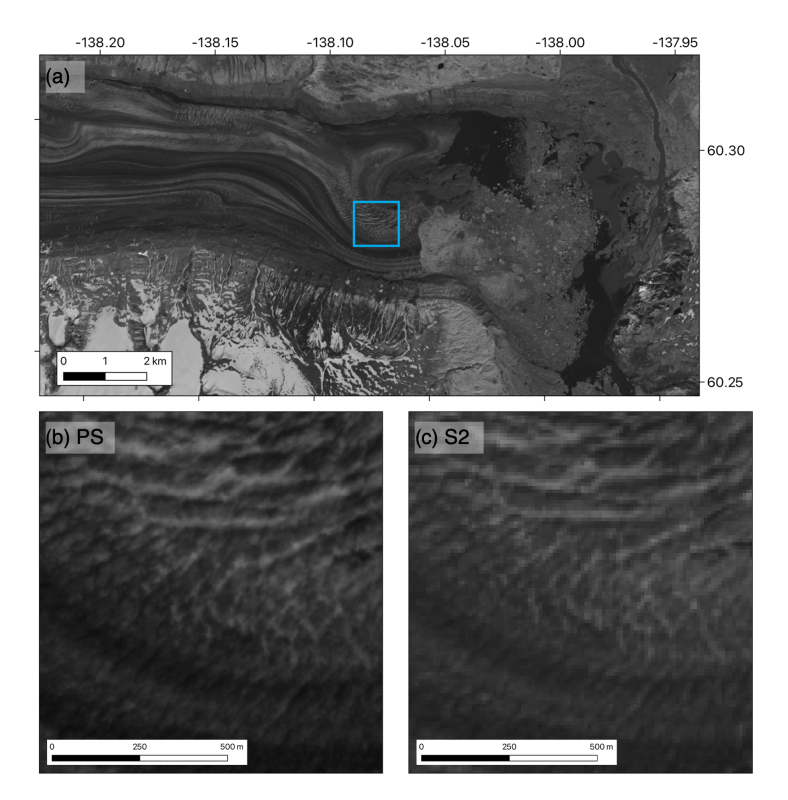


Figure A4. Comparison of a 5 m resolution PS image from 4 July 2020 (b) and a 10 m resolution S2 image from 1 July 2020 (c) over an area in the southern split of LO's terminus, marked by the blue box in panel (a).

Code and data availability. The PlanetScope image pre-processing pipeline has been released on GitHub as planet_tile2img (https://doi.org/10.5281/zenodo.10632745, Liu et al., 2024b), and the custom autoRIFT code is included as the CautoRIFT GitHub repository: https://doi.org/10.5281/zenodo.11372310 (Liu, 2024). Data for the paper are published through the NSIDC: https://doi.org/10.5067/VHFVXHZHOO6P (Liu et al., 2024c).

Author contributions. JL, MG, and RA contributed code to the PlanetScope image pre-processing pipeline. MG and JL collected and managed the data. JL and EE designed the study and defined the scope and applications. JL wrote the manuscript and generated the figures. All authors contributed to the revision of the final paper and figures.

Competing interests. The contact author has declared that none of the authors has any competing interests.

Disclaimer. Publisher's note: Copernicus Publications remains neutral with regard to jurisdictional claims made in the text, published maps, institutional affiliations, or any other geographical representation in this paper. While Copernicus Publications makes every effort to include appropriate place names, the final responsibility lies with the authors.

Acknowledgements. This research was funded by the NASA FI-NESST Award 80NSSC21K1640, NSF Award ANS1954006, and the Department of Defense SMART Scholarship. We are grateful to Editor Daniel Farinotti, to Robert McNabb, and to a second, anonymous reviewer for their valuable feedback throughout the peer review process. T. Dylan Mikesell, Hans-Peter Marshall, and Christine Dow provided additional commentary on the paper that aided its revision.

Financial support. This research has been supported by the National Aeronautics and Space Administration (grant no. 80NSSC21K1640) and the National Science Foundation (grant no. ANS1954006).

Review statement. This paper was edited by Daniel Farinotti and reviewed by Robert McNabb and one anonymous referee.

References

- Abe, T. and Furuya, M.: Winter speed-up of quiescent surgetype glaciers in Yukon, Canada, The Cryosphere, 9, 1183–1190, https://doi.org/10.5194/tc-9-1183-2015, 2015.
- Beaud, F., Aati, S., Delaney, I., Adhikari, S., and Avouac, J.-P.: Surge dynamics of Shisper Glacier revealed by time-series correlation of optical satellite images and their utility to substanti-

- ate a generalized sliding law, The Cryosphere, 16, 3123–3148, https://doi.org/10.5194/tc-16-3123-2022, 2022.
- Benn, D. I., Hewitt, I. J., and Luckman, A. J.: Enthalpy balance theory unifies diverse glacier surge behaviour, Ann. Glaciol., 63, 88–94, https://doi.org/10.1017/aog.2023.23, 2023.
- Bhambri, R., Hewitt, K., Haritashya, U. K., Chand, P., Kumar, A., Verma, A., Tiwari, S. K., and Rai, S. K.: Characteristics of surge-type tributary glaciers, Karakoram, Geomorphology, 403, 108161, https://doi.org/10.1016/j.geomorph.2022.108161, 2022.
- Burgess, E. W., Larsen, C. F., and Forster, R. R.: Summer melt regulates winter glacier flow speeds throughout Alaska, Geophys. Res. Lett., 40, 6160–6164, https://doi.org/10.1002/2013GL058228, 2013.
- Fountain, A. G. and Walder, J. S.: Water flow through temperate glaciers, Rev. Geophys., 36, 299–328, https://doi.org/10.1029/97RG03579, 1998.
- Frazier, A. E. and Hemingway, B. L.: A Technical Review of Planet Smallsat Data: Practical Considerations for Processing and Using PlanetScope Imagery, Remote Sens., 13, 3930, https://doi.org/10.3390/rs13193930, 2021.
- Gardner, A. S., Moholdt, G., Scambos, T., Fahnstock, M., Ligtenberg, S., van den Broeke, M., and Nilsson, J.: Increased West Antarctic and unchanged East Antarctic ice discharge over the last 7 years, The Cryosphere, 12, 521–547, https://doi.org/10.5194/tc-12-521-2018, 2018.
- Gardner, A. S., Fahnestock, M. A., and Scambos, T. A.: MEaSURES ITS_LIVE Landsat Image-Pair Glacier and Ice Sheet Surface Velocities: Version 1. Data archived at National Snow and Ice Data Center [data set], https://doi.org/10.5067/IMR9D3PEI28U, 2023.
- Herreid, S. and Truffer, M.: Automated detection of unstable glacier flow and a spectrum of speedup behavior in the Alaska Range, J. Geophys. Res.-Earth Surf., 121, 64–81, https://doi.org/10.1002/2015JF003502, 2016.
- Howat, I.: MEaSUREs Greenland Ice Velocity: Selected Glacier Site Velocity Maps from Optical Images, Version 3, Boulder, Colorado USA, NASA National Snow and Ice Data Center Distributed Active Archive Center [data set], https://doi.org/10.5067/RRFY5IW94X5W, 2020.
- Jiang, Z., Wu, K., Liu, S., Wang, X., Zhang, Y., Tahir, A. A., and Long, S.: Surging dynamics of South Rimo Glacier, Eastern Karakoram, Environ. Res. Lett., 16, 114044, https://doi.org/10.1088/1748-9326/ac3175, 2021.
- King, M. D., Howat, I. M., Candela, S. G., Noh, M. J., Jeong, S., Noël, B. P. Y., van den Broeke, M. R., Wouters, B., and Negrete, A.: Dynamic ice loss from the Greenland Ice Sheet driven by sustained glacier retreat, Commun. Earth Environ., 1, 1, https://doi.org/10.1038/s43247-020-0001-2, 2020.
- Kington, J. and Collison, A.: Scene Level Normalization and Harmonization of Planet Dove Imagery, https://assets.planet.com/docs/scene_level_normalization_of_planet_dove_imagery.pdf (last access: 8 August 2024), 2022.
- Landa, M., Neteler, M., Metz, M., Petrasova, A., Petras, V., Cho, H., Delucchi, L., Barton, M., Chemin, Y., Zigo, T., and Kudrnovsky, H.: GRASS GIS 7.8.6RC2 (7.8.6RC2), Zenodo [code], https://doi.org/10.5281/zenodo.5176031, 2021.
- Latte, N. and Lejeune, P.: PlanetScope Radiometric Normalization and Sentinel-2 Super-Resolution (2.5 m): A Straightforward Spectral-Spatial Fusion of Multi-Satellite Multi-Sensor Images

- Using Residual Convolutional Neural Networks, Remote Sens., 12, 2366, https://doi.org/10.3390/rs12152366, 2020.
- Leach, N., Coops, N. C., and Obrknezev, N.: Normalization method for multi-sensor high spatial and temporal resolution satellite imagery with radiometric inconsistencies, Comput. Electron. Agric., 164, 104893, https://doi.org/10.1016/j.compag.2019.104893, 2019.
- Lei, Y., Gardner, A., and Agram, P.: Autonomous Repeat Image Feature Tracking (autoRIFT) and Its Application for Tracking Ice Displacement, Remote Sens., 13, 749, https://doi.org/10.3390/rs13040749, 2021.
- Li, J. and Roy, D. P.: A Global Analysis of Sentinel-2A, Sentinel-2B and Landsat-8 Data Revisit Intervals and Implications for Terrestrial Monitoring, Remote Sens., 9, 902, https://doi.org/10.3390/rs9090902, 2017.
- Liu, J.: jukesliu/CautoRIFT: v1.1.1 (1.1.1), Zenodo [code], https://doi.org/10.5281/zenodo.11372310, 2024.
- Liu, J., Enderlin, E. M., Bartholomaus, T., Terleth, Y., Mikesell, T., and Beaud, F.: Propagating speedups during quiescence escalate to the 2020-2021 surge of Sít' Kusá, southeast Alaska, J. Glaciol., published online, 1–12, https://doi.org/10.1017/jog.2023.99, 2024a.
- Liu, J., Gendreau, M., Enderlin, E., and Aberle, R.: CryoGARS-Glaciology/planet_tile2img: Initial release (v0.1.1), Zenodo [code], https://doi.org/10.5281/zenodo.10632745, 2024b.
- Liu, J., Gendreau, M., Enderlin, E. M., and Aberle, R.: Custom autoRIFT velocity maps, NSIDC [data set], https://doi.org/10.5067/VHFVXHZHOO6P, in review, 2024c.
- Marin, C., Bertoldi, G., Premier, V., Callegari, M., Brida, C., Hürkamp, K., Tschiersch, J., Zebisch, M., and Notarnicola, C.: Use of Sentinel-1 radar observations to evaluate snowmelt dynamics in alpine regions, The Cryosphere, 14, 935–956, https://doi.org/10.5194/tc-14-935-2020, 2020.
- Meyer, C. R. and Minchew, B. M.: Temperate ice in the shear margins of the Antarctic Ice Sheet: Controlling processes and preliminary locations, Earth Planet. Sci. Lett., 498, 17–26, https://doi.org/10.1016/j.epsl.2018.06.028, 2018.
- Nanni, U., Scherler, D., Ayoub, F., Millan, R., Herman, F., and Avouac, J.-P.: Climatic control on seasonal variations in mountain glacier surface velocity, The Cryosphere, 17, 1567–1583, https://doi.org/10.5194/tc-17-1567-2023, 2023.
- Nolan, A., Kochtitzky, W., Enderlin, E. M., McNabb, R., and Kreutz, K. J.: Kinematics of the exceptionally-short surge cycles of Sít' Kusá (Turner Glacier), Alaska, from 1983 to 2013, J. Glaciol., 67, 744–758, https://doi.org/10.1017/jog.2021.29, 2021
- Paul, F., Piermattei, L., Treichler, D., Gilbert, L., Girod, L., Kääb, A., Libert, L., Nagler, T., Strozzi, T., and Wuite, J.: Three different glacier surges at a spot: what satellites observe and what not, The Cryosphere, 16, 2505–2526, https://doi.org/10.5194/tc-16-2505-2022, 2022.

- PBC, P. L.: Planet Imagery Product Specifications, https://assets.planet.com/docs/Planet_Combined_Imagery_ Product_Specs_letter_screen.pdf (last access: 8 August 2024), 2022
- Ranganathan, M., Barotta, J.-W., Meyer, C. R., and Minchew, B.: Meltwater generation in ice stream shear margins: case study in Antarctic ice streams, P. Roy. Soc. A, 479, 20220473, https://doi.org/10.1098/rspa.2022.0473, 2023.
- Roy, D. P., Huang, H., Houborg, R., and Martins, V. S.: A global analysis of the temporal availability of PlanetScope high spatial resolution multi-spectral imagery, Remote Sens. Environ., 264, 112586, https://doi.org/10.1016/j.rse.2021.112586, 2021.
- Sommervold, O., Gazzea, M., and Arghandeh, R.: A Survey on SAR and Optical Satellite Image Registration, Remote Sens., 15, 850, https://doi.org/10.3390/rs15030850, 2023.
- Summers, P. T., Elsworth, C. W., Dow, C. F., and Suckale, J.: Migration of the Shear Margins at Thwaites Glacier: Dependence on Basal Conditions and Testability Against Field Data, J. Geophys. Res.-Earth Surf., 128, e2022JF006958, https://doi.org/10.1029/2022JF006958, 2023.
- Terleth, Y., Bartholomaus, T. C., Liu, J., Beaud, F., Mikesell, T. D., and Enderlin, E. M.: Transient subglacial water routing efficiency modulates ice velocities prior to surge termination on Sít' Kusá, Alaska, J. Glaciol., published online, 1–17, https://doi.org/10.1017/jog.2024.38, 2024.
- Van Wychen, W., Bayer, C., Copland, L., Brummell, E., and Dow, C.: Radarsat Constellation Mission Derived Winter Glacier Velocities for the St. Elias Icefield, Yukon/Alaska: 2022 and 2023, Can. J. Remote Sens., 49, 2264395, https://doi.org/10.1080/07038992.2023.2264395, 2023.
- Van Wyk de Vries, M. and Wickert, A. D.: Glacier Image Velocimetry: an open-source toolbox for easy and rapid calculation of high-resolution glacier velocity fields, The Cryosphere, 15, 2115–2132, https://doi.org/10.5194/tc-15-2115-2021, 2021.
- Van Wyk de Vries, M., Bhushan, S., Jacquemart, M., Deschamps-Berger, C., Berthier, E., Gascoin, S., Shean, D. E., Shugar, D. H., and Kääb, A.: Pre-collapse motion of the February 2021 Chamoli rock—ice avalanche, Indian Himalaya, Nat. Hazards Earth Syst. Sci., 22, 3309–3327, https://doi.org/10.5194/nhess-22-3309-2022, 2022.
- Working Group on the Randolph Glacier Inventory and Infrastructure for Glacier Monitoring: Randolph Glacier inventory A dataset of global glacier outlines: Version 6.0: Technical report, Global Land Ice Measurements from Space [data set], https://doi.org/10.7265/N5-RGI-60, 2017.